

# Electro-osmosis-driven micro-channel flows: A comparative study of microscopic particle image velocimetry measurements and numerical simulations

M. J. Kim, A. Beskok, K. D. Kihm

170

**Abstract** This paper presents global and point-wise comparisons of experimental measurements and numerical simulation results of electro-osmotically driven flows in two elementary micro-channel configurations, a straight channel with a groove and a T-junction channel. The micro-channels are made by photolithography using poly-dimethylsiloxane (PDMS), a type of silicon product, which is transparent, and electro-osmotically permeable to a variety of liquids. A microscopic particle image velocimetry system has been developed to measure full field velocity distributions by tracking the fluorescence images of 500-nm diameter fluorescein dye particles. The numerical algorithm is based on a spectral element formulation of incompressible Navier–Stokes equations with electro-osmotic forcing. The algorithm utilizes modal expansions in mixed quadrilateral and triangular meshes, enabling complex geometry discretizations with spectral accuracy. Comparisons of experimental and numerical results show good agreements, validating both numerical and experimental methodologies.

## 1 Introduction

Electro-osmosis is the process of inducing motion of ionized liquid, adjacent to a stationary charged surface, under an applied external electric field. Electro-osmosis has strong potential for use in microfluidic systems in that fluid pumping, handling, and control can be achieved through selective applications of electric fields, eliminating moving mechanical components such as valves and flow switches. In microscales, electro-osmosis can replace pressure-driven flows and alleviate the difficulties associated with exceedingly large pressure gradients occurring with mechanical pumping for microscale channels.

Liquid flows in capillary porous systems under the influence of external electric fields have attracted the atten-

tion of many scientists, since the discovery of electrokinetic transport by Reuss in 1809 (Probstein 1994). In 1870, Helmholtz developed the electric double layer theory, which relates the electrical and flow parameters for electrokinetic transport. In the late 1930s, electro-osmosis began to be widely used particularly for chemistry applications. Recent theoretical developments include solution of mixed electro-osmotic/pressure-driven flows in very thin two-dimensional slits (Burgreen and Nakache 1964; Ohshima and Kondo 1990; Dutta and Beskok, 2001a), as well as in thin cylindrical capillaries (Rice and Whitehead 1965). In 1952, Overbeek proposed the irrotationality of internal electro-osmotic flows for arbitrarily shaped geometries. This is followed by the ideal electro-osmosis concept (i.e., electro-osmotic flow in the absence of externally imposed pressure forces) by Cummings et al. (1999), who showed the similarity between the electric and the velocity fields, irrespective of the Reynolds number. More recently, Santiago (2001) has shown that ideal electro-osmosis is observed for low Reynolds number, steady flows. However, unsteady or high Reynolds number flows violate this condition. Analytical solution of unsteady electro-osmotic flows confirm the predictions of Santiago (Dutta and Beskok 2001b).

Experimental measurements of electrokinetically driven micro-flows have been attempted in a number of previous works. Meinhart et al. (1999) presented PIV measurements of a micro-channel flow. In their study, accuracy of the PIV system was demonstrated by measuring a pressure-driven flow field in a  $30\ \mu\text{m} \times 300\ \mu\text{m} \times 25\ \text{mm}$  rectangular glass micro-channel. Flow patterns for electro-osmotically driven flows were obtained using an Ar-ion laser PIV (Cummings et al. 1999). Herr et al. (2000) investigated the velocity profile of flows under electrokinetic transport with a high-resolution caged fluorescence imaging technique.

There has been a growing interest in numerical simulation of electrokinetically driven micro-flows. Recently, liquid flow and forced convection heat transfer in electro-osmotically driven micro-channels were analyzed using a finite difference method (Mala et al. 1997; Yang and Li 1998). Micro-injection through the intersection of two-channels has been studied using a finite volume formulation based on the Debye–Hückel linearization (Patankar and Hu 1998). Electro-osmotic and electrophoretic transport in two-dimensional complex geometry flow conduits has been analyzed using a finite difference algorithm (Ermakov et al. 1998). Electro-osmotically driven micro-flows in T-junctions were investigated by a finite element formulation (Bianchi et al. 2000), also by using a meshless

Received: 1 February 2002 / Accepted: 19 March 2002  
Published online: 8 May 2002  
© Springer-Verlag 2002

M. J. Kim, A. Beskok, K. D. Kihm (✉)  
Department of Mechanical Engineering,  
Texas A&M University, College Station, TX 77843-3123, USA  
E-mail: ken-kih@tamu.edu  
Tel.: +1-979-8452143  
Fax: +1-979-8622418

The authors acknowledge Dr. Prashanta Dutta and Mr. Jungyoon Hahm for their assistance with the numerical simulations. Support from the TAMU Interdisciplinary Research Program is acknowledged and appreciated for the present work.

finite cloud algorithm (Mitchell et al. 2000). Electro-osmotic flow control in cross-channels and T-junctions were investigated using a spectral element formulation, and flow control with multiple electric fields was demonstrated (Dutta et al. 2002a, 2002b).

Most of the previous research concentrated on either experimental measurements or numerical simulation of electro-osmotic flows. Quantitative comparisons of experimental data and numerical predictions have been presented in very limited studies. We therefore introduce here a combined experimental/numerical study of electro-osmotic transport in two representative elementary configurations, namely, a grooved micro-channel and a T-junction micro-channel. Our objective is to outline the challenges of experimentation and modeling of electrokinetic transport in micro-scales, and present the limitations involved in comparisons of two-dimensional numerical results with the microscopic particle image velocimetry ( $\mu$ -PIV) data. Through this study, we also establish benchmarks for validation of both the numerical models and the  $\mu$ -PIV technique, by presenting quantitative global and point-wise comparisons between the experiments and numerical results.

This paper is organized as follows: we first present the basic theory for electrokinetic transport, followed by the micro-channel fabrication, the experimental setup, and the numerical formulation sections. In the results section, we present the global and point-wise comparisons between the numerical and experimental results for both the grooved micro-channel and the T-junction micro-channel. Finally, conclusive remarks are presented, including a possible future research direction.

## 2

### Modeling of electro-osmotic transport

Formation of an electric double layer (EDL) plays a key role in all electrokinetic transport processes (Fig. 1). For

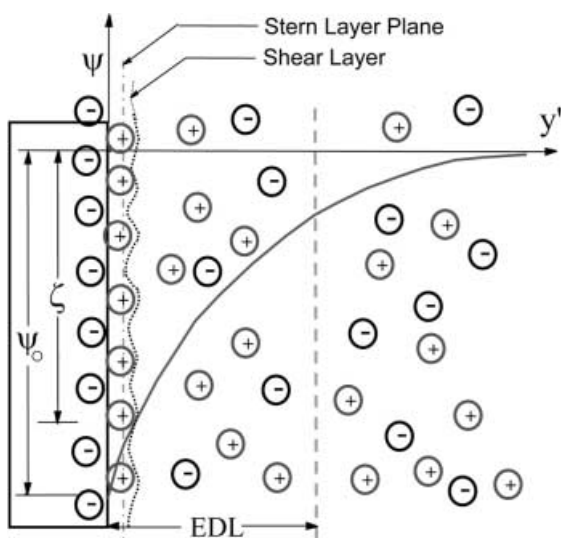


Fig. 1. Schematic diagram of EDL next to a negatively charged solid surface. Here,  $\psi$  is the electro-osmotic potential,  $\psi_0$  is the surface potential,  $\zeta$  is the zeta potential, and  $y'$  is the distance measured from the wall

example, when silica is in contact with an aqueous solution, its surface hydrolyzes to form silanol surface groups (Probstein 1994). These groups may be positively charged as  $\text{SiOH}_2^+$ , neutral as  $\text{SiOH}$ , or negatively charged as  $\text{SiO}^-$ , depending on the pH value of the electrolyte solution. If the channel surface is negatively charged (such as in the case of deionized water), the positive ions are attracted towards the surface, and the negative ions are repelled from the surface, keeping the bulk of the electrically neutral liquid far away from the wall. The distance from the wall, where the electro-osmotic potential energy is equal to the thermal energy is known as the Debye length ( $\lambda$ ). Ion redistribution within the Debye length results in a net electric charge, which is characterized by the electro-osmotic potential. This region is also known as the EDL, which consists of two distinct zones: Stern- and diffuse-layers. The Stern layer is formed owing to strong attraction of ions onto the oppositely charged wall surface. The ions are immobilized near the charged surfaces, and the electro-osmotic potential drops rapidly across the Stern-layer to a value at the edge of the Stern-layer, known as the zeta potential ( $\zeta$ ). The zeta potential, along with the buffer ion concentration, characterizes the electro-osmotic transport.

Electro-osmotic potential distribution in the diffuse-layer is governed by the Poisson-Boltzmann equation,

$$\nabla^2 \psi = -\frac{\rho_e}{\epsilon}, \quad (1)$$

where  $\psi$  is the electro-osmotic potential,  $\rho_e$  is the charge density, and  $\epsilon$  is the electric permittivity.

For a symmetric electrolyte under equilibrium distribution, the charge density is given by the Boltzmann distribution, resulting in:

$$\rho_e = -2n_0 e z \sinh(ez\psi/k_B T), \quad (2)$$

where  $e$  is the electron charge,  $z$  is the valence,  $k_B$  is the Boltzmann constant,  $n_0$  is the ion density of the bulk solution, and  $T$  is the temperature.

The Debye length ( $\lambda$ ) depends on the molar concentration ( $n_0$ ) of the ionized fluid, and it can be estimated using the Debye-Hückel parameter ( $\omega$ ) as:

$$\omega = \frac{1}{\lambda} = \sqrt{\frac{2n_0 e^2 z^2}{\epsilon k_B T}}. \quad (3)$$

Using this equation, one obtains Debye lengths of  $\lambda = 3$  nm, 100 nm, and 300 nm, for  $n_0 = 1.0 \times 10^{-2}$ ,  $1.0 \times 10^{-5}$ , and  $1.0 \times 10^{-6}$  M, respectively. The characteristic channel dimensions ( $h$ ) utilized in microfluidics are on the order of  $10 \sim 100$   $\mu\text{m}$ . Comparisons of the typical Debye lengths with the aforementioned micro-channel dimensions show a one to five order-of-magnitudes difference between these two length scales.

Electro-osmotic flow is generated by the interaction of the external electric field with the net charge distribution in the EDL. For the case of the negatively charged surface, for example, the EDL becomes positively charged. Application of an external electric field  $\vec{E}$  mobilizes the ions in the EDL, resulting in motion towards the cathode. Bulk

flow motion is determined from the incompressible Navier–Stokes equations:

$$\rho_f \left( \frac{\partial \vec{v}}{\partial t} + (\vec{v} \cdot \nabla) \vec{v} \right) = -\nabla P + \mu \nabla^2 \vec{v} + \rho_e \vec{E} \quad (4)$$

where  $\rho_f$  is fluid density,  $\mu$  is the absolute viscosity,  $P$  is the pressure, and  $\vec{v}$  is a divergence free velocity field ( $\nabla \cdot \vec{v} = 0$ ). The term  $\rho_e \vec{E}$  shows the electrokinetic body forces. Equation 4 is subject to no-slip boundary conditions on all solid surfaces. The externally applied electric field is given by

$$\vec{E} = -\nabla \phi \quad (5)$$

where  $\phi$  is the electric potential governed by the law of electrostatics:

$$\nabla \cdot (\sigma \nabla \phi) = 0 \quad (6)$$

where  $\sigma$  is the electric conductivity. The externally applied electric field is subject to insulating boundary conditions on dielectric surfaces, i.e.,  $\partial \phi / \partial n = 0$ . Equations 1, 2, 3, 4, 5 and 6 assume Newtonian fluid with viscosity and permittivity independent of the local or overall electric field. This is a valid approximation for dilute solutions. The ions are point charges, and negligible ion-convection effects compared with the ion-diffusion are also assumed.

Velocity distribution for electro-osmotically-driven straight channel flows can be obtained by assuming steady, fully developed flow with zero pressure gradients, in which Eq. 4 retains only the driving electrokinetic force and the cross-channel diffusion terms. For the case when the EDL thickness is significantly smaller than the channel dimensions, a plug-like velocity is observed in the bulk of the channel, which is also known as the Helmholtz–Smoluchowski electro-osmotic velocity, given by

$$U_{HS} = \frac{-\zeta \epsilon E_x}{\mu}, \quad (7)$$

where  $E_x$  is the applied electric field in the streamwise direction, and  $\mu$  is absolute fluid viscosity. The zeta potential can now be experimentally estimated from the measured plug velocity  $U_{HS}$ , and the specified electric field  $E_x$ .

### 3 Fabrication of micro-channels

Recent developments in micro-fabrication technologies have enabled a variety of miniaturized fluidic systems consisting of micro-ducts, valves, pumps, and various other injection systems. Fabrication techniques, such as surface silicon micromachining, bulk silicon micromachining, lithographic galvanofarming (LIGA), chemical wet etching, anodic bonding, and electro discharge machining (EDM) are successfully applied to build these micro-fluidic and other microelectromechanical systems devices. Two of the most recent micro-fabrication techniques are ultraviolet laser ablation (UVLA) using organic polymeric substrate (Bianchi et al. 2001), and photolithography using poly-dimethylsiloxane (PDMS) (Anderson et al. 2000). In UVLA, micro-channels of different dimensions and geometries can be easily

obtained by varying the UV laser ablation parameters, such as substrate translation speed, laser energy flux, pulse repetition rate, and mask shape.

In the current work, we utilized PDMS (Dow Corning Sylgard Silicone Elastomer-184, Krayden Inc., Houston, Tex.) material to fabricate micro-channels by using photolithography, primarily because of the simplicity and local affordability of its fabrication facility at our laboratory. The PDMS is made by combining methyl chloride with silicon. It is transparent, viable to EDL development in contact with water and other aqueous solutions, and it has low surface energy for good wetting. Fabrication of micro-fluidic devices in PDMS by the replica molding method can provide faster and less complicated fabrication processes than glass/silicone etching with anodic bonding techniques.

Figure 2 shows the micro-fabrication sequence of micro-channel geometry. Fabrication starts with substrate insulation by thermal oxidation of microslide in the wet oxide furnace. Then photoresist (Microposit 1813, Shipley Inc., Marlborough, Mass.) is spin-coated on a planar glass substrate to form a uniform thickness of 5–50  $\mu\text{m}$ , inversely depending on the spinning speed. The next step is to etch a channel manifold on the substrate using the photolithography technique to generate a protective mask. A mask, made out of a high-resolution photographic negative film printed to scale is put on the substrate, and then a UV beam (300~350 nm) is illuminated for a specified duration to make a positively etched channel manifold. After this process, the excess photoresist is carefully peeled off from the glass substrate and washed repeatedly with acetone and ethanol. This results in a glass substrate that has the positive pattern of the master. In the meantime, an elastomeric mold is made by curing low molecular weight polymer (PDMS) with a cross-linker on a

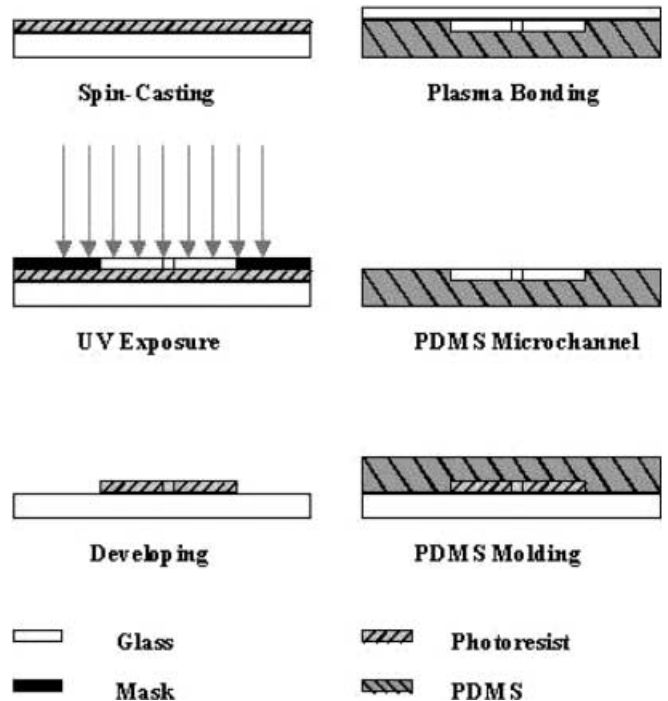


Fig. 2. Micro-channel fabrication processes using PDMS

photolithographically patterned master that is prepared by exposing and developing a photoresist patterned surface and baking in a kiln at 80°C for about 6 h, which solidifies the PDMS mold.

Finally, the PDMS surface is rendered hydrophilic by oxygen plasma treatment for 20 s (Plasma cleaner PDC-32G, Harrick Scientific, Ossining, NY) before bonding with a glass cover slip. The glass cover slips used in micro-fabrication have been cleaned in hot surfactant solution (ICN×7 detergent, Costa Mesa, CA) and rinsed at least 20 times in purified water using a NANO Pure ultrapure water system (Barnstead, Dubuque, IA). It is then baked in a kiln at 400°C for 4 h before use. The fabricated channels are 300 μm wide, and 7 μm deep for both the grooved- and T-junction configurations.

#### 4 Experimental setup

We developed a μ-PIV system to measure electro-osmotic/pressure-driven flows in various micro-channel configurations (Fig. 3). The use of the μ-PIV enables spatially resolved measurements of instantaneous velocity fields. The liquid flow in micro-channels is monitored from the fluorescence of the seeded dye molecules. Traditional epi-illumination fluorescence microscopy is used by placing the micro-channels on the microscope stage with the glass slide facing towards the objective lens.

The μ-PIV utilizes flow-tracing particles to map the flow in the micro-geometries. In this study we used 500 nm fluorescent micro-spheres (Molecular Probes, Inc., Eugene, Ore.) that have an excitation peak at 490 nm and an emission peak at 515 nm. The concentration of fluorescent micro-spheres based on the interrogation volume is  $7.26 \times 10^8$  particles/ml, or 0.196% in volume fraction. A 40-mW “Blue” Ar-ion CW laser beam (488 nm) is used to pump the fluorescent seeding particles. A laser beam is

passed through a beam expander to enlarge the beam diameter, and then collimated to illuminate the test section of the micro-channel. A 10× objective lens is used for magnification of the images, and the field of view of our experiment is approximately 1 mm×750 μm. The fluorescence signal is recorded with an interline transfer CCD monochrome camera (Sony XC-73, Edmund Industrial Optics, NJ). The linearity of the camera response to light intensity is checked by flooding the device with different concentrations of fluorescent micro-spheres. We captured 20 images/s and used 640×480 pixels video format with the CCD monochrome camera. In the PIV image processing, the spatial resolution is 16×16 pixels and the interrogation cell overlay is given as 50%. Ensemble averaging of up to 80 images consecutively captured for 4 s is used to obtain the velocity measurements.

#### 4.1 Dynamic velocity range and dynamic spatial range of μ-PIV

The spatial resolution of a micro-PIV system is limited by the diffraction limit of particle images and numerical aperture (NA) of the objective lens. Assuming that a point spread function describes the small particle images, which is analogous to the diffraction pattern of a point source of light, the characteristic diameter of a point-spread function  $d_s$  (Born and Wolf 1965) is given as,

$$d_s = 1.22(1 + M)\lambda NA^{-1} \approx 26 \mu\text{m} \quad (8)$$

where the objective magnification is  $M=10$ , the wavelength of the illuminating light  $\lambda=488$  nm, and the numerical aperture  $NA=0.25$ . The actual image on the CCD camera is known to be the convolution of the diffraction limited image with the geometric image (Adrian 1997). Assuming the geometric and diffraction limited images as Gaussian functions, an effective image diameter  $d_e$  is given for  $d_p=500$ -nm particle diameter as

$$d_e = [M^2 d_p^2 + d_s^2]^{1/2} \approx 26.7 \mu\text{m} \quad (9)$$

The dynamic velocity range (DVR) is estimated following the formula derived by Adrian (1997),

$$DVR = \frac{u_{\max} M \Delta t}{0.04(d_e^2 + d_r^2)^{1/2}} \approx 160 \quad (10)$$

where the (measured) maximum velocity is given as  $u_{\max}=360$  μm/s, for the case of the grooved channel (Fig. 6), the image frame interval  $\Delta t=0.05$  s (20 fps), and the CCD pixel size  $d_r \approx 9.0$  μm. This calculation shows an estimation of the minimum detectable velocity of approximately 2.25 μm/s for our μ-PIV system. The minimum velocity magnitude is measured as 2.49 μm/s for the case of the grooved channel. For the case of the T-junction (Fig. 9), the measured maximum, minimum detectable, and minimum measured velocities are 401 μm/s, 2.50 μm/s, and 5.83 μm/s.

Dynamic spatial range (DSR) is defined as the ratio of the maximum resolvable scale to the minimum resolvable scale, and this ratio is equivalent to the ratio of the

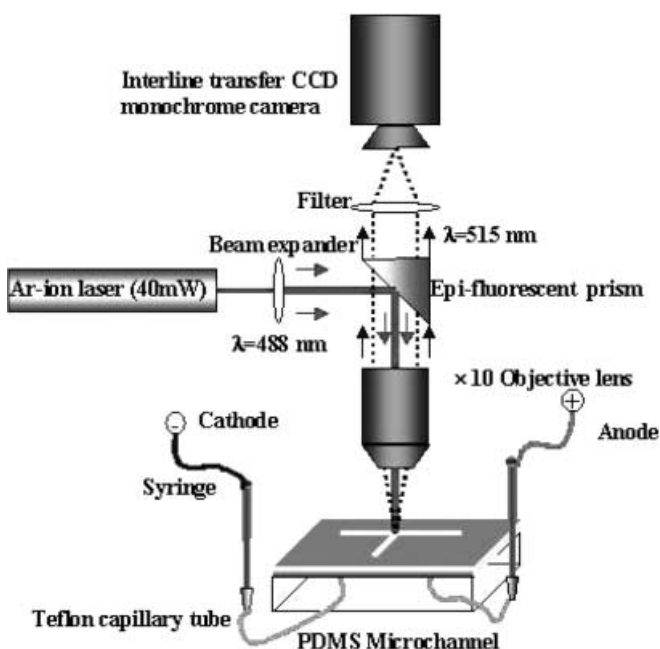


Fig. 3. Experimental set-up of μ-PIV system

field-of-view length to the maximum flow displacement as also given by (Adrian 1997):

$$DSR = \frac{l_{fov}}{\Delta x_{max}} = \frac{L_x/M}{u_{max}\Delta t} \approx 36 \quad (11)$$

where the CCD array dimension is  $L_x=6.40$  mm. Therefore, for the present field-of-view,  $l_{fov}=1$  mm by  $750 \mu\text{m}$ , the minimum resolvable scale is estimated to  $\Delta x_{max}\approx 23.5 \mu\text{m}$  on average. In practice, the data resolution is equivalent to the PIV interrogation window size of  $25\text{-}\mu\text{m}$  square, and this is approximately the same as the estimated resolvable scale.

## 4.2 Image depth of field

The depth of field of the microscope objective lens defines the image plane for  $\mu$ -PIV. Microscope objectives usually have very thin depths of field and the resulting  $\mu$ -PIV image plane thickness is much narrower than conventional PIV image planes that are defined by a thin laser sheet of generally a few hundred micron in thickness. Considering diffraction and geometric affects, Inoue and Spring (1997) reported the formulation for depth of field as

$$\delta z = \frac{n\lambda}{NA^2} + \frac{nd_r}{MNA} \quad (12)$$

where the index of refraction of medium is  $n=1.0$ , the wavelength of illuminating light  $\lambda=488$  nm, the numerical aperture  $NA=0.25$ , the magnification is  $M=10$ , and the CCD pixel size is  $d_r\approx 9.0 \mu\text{m}$ . Thus, the depth of field of the present  $\mu$ -PIV system is estimated to be  $\delta z=11.4 \mu\text{m}$ . Since this depth of field exceeds the fabricated channel depth of  $7 \mu\text{m}$ , the PIV images effectively represent the depthwise average of the entire  $7\text{-}\mu\text{m}$ -deep channel flow. For the case of the channel depths far exceeding the depth of field, an in-depth analysis and rigorous discussions are reported for the contribution of out-of-focus particle images to the PIV correlation functions by Olsen and Adrian (2000).

## 4.3 Measurement error from Brownian motion

The thermal Brownian diffusive motion may not be negligible when sub-micron particles are used for seeding, since the particle diffusivity rapidly increases with decreasing particle diameter. The average particle displacement by the Brownian motion during an elapsed time interval is given as  $\bar{x} \approx \sqrt{2D\Delta t}$  (Einstein 1905) and the Brownian velocity is estimated as

$$u_B = \sqrt{\frac{2D}{\Delta t}} \quad (13)$$

where the diffusivity of  $500\text{-nm}$  particles suspended in water at  $20^\circ\text{C}$  (Friedlander 1977) is given as

$$D = \frac{kT}{3\pi\mu d_p} \approx 8.58 \times 10^{-9} \text{ cm}^2/\text{s} \quad (14)$$

and the resulting Brownian velocity is calculated as  $u_B=5.86 \mu\text{m/s}$  for  $20$  frames/s imaging, or  $\Delta t=0.05$  s.

The Brownian motion error,  $\epsilon_B \equiv u_B/u$  ( $u$ =characteristic velocity), is considered as having the same effect in all directions statistically. If one assumes that each particle has equal influence on the average velocity vector in the interrogation window,  $\epsilon_B$  can be reduced by averaging the number of individual particle images within the interrogation window,  $M$ , and ensemble averaging over the number of realizations,  $N$ . The Brownian motion error for PIV recording (Santiago et al. 1998) is expressed as

$$\epsilon_B = \frac{u_B}{u} \frac{1}{\sqrt{M \times N}} \quad (15)$$

For example, for a characteristic velocity of  $100 \mu\text{m/s}$  from averaging of  $20$  image and for five pairs of particle images within a single interrogation window, the Brownian motion error is estimated to be as little as  $0.6\%$ .

## 5 Numerical simulation

We used a spectral element method for solution of the Poisson–Boltzmann equation (Eq. 6) and the incompressible Navier–Stokes equations. The numerical algorithm employs modal spectral expansions in quadrilateral and unstructured triangular meshes. This allows discretization of complex engineering geometries with great flexibility (due to the unstructured grid) and maintains high-order numerical accuracy. The Poisson–Boltzmann equation is solved in weak variational form using a Galerkin projection. Its exponential non-linearity is handled by Newton iterations. Details of numerical discretizations and code validation are given in Dutta et al. (2002a).

There are drastic length-scale differences between the EDL thickness ( $\lambda$ ) and micro-channel dimensions ( $h$ ). Since the flow is driven by the electro-osmotic body forces concentrated within the EDL, numerical models which resolve the EDL region are faced with a *numerical stiffness* due to the disparity between the length scales. Despite the fact that the EDL can be one to five orders of magnitude smaller than the micro-channel dimensions, most published numerical simulation works utilize a tolerable value of  $\lambda/h=0.01$  (Patankar and Hu 1998; Nann and Heinze 1999; Bianchi et al. 2000; Mitchell et al. 2000).

Questions may arise with regard to the effect of this length-scale disparity for comparisons between the experimental data and numerical simulations. In Dutta and Beskok (2001a), it is analytically shown that the EDL thickness does not affect the bulk flow region for steady Stokes flows, as long as the EDL is sufficiently smaller than the channel thickness ( $\lambda/h \leq 0.01$ ). The effects of EDL on velocity and vorticity distribution are felt up to a distance of  $\delta_{99}\times\lambda$  from the walls, where  $\delta_{99}$  is the effective EDL thickness, defined as a function of the zeta potential and fluid temperature. At a room temperature of  $300$  K, for example,  $\delta_{99}<4.5$  for  $\zeta>25$  mV and higher. Therefore, comparisons between the experimental and numerical results are performed by matching the geometry, electric field, and the Reynolds number. However, complete similarity is not possible due to the aforementioned inconsistency in intrinsic nondimensional length scale ( $\lambda/h$ ).

Physically, the numerical simulations correspond to electrokinetic transport at lower buffer concentrations with larger EDL thickness, in comparison with the corresponding experimental conditions. Nevertheless, since the EDL thickness does not affect the bulk flow region, we present comparisons between the experiments and simulation in the bulk flow region.

Note that numerical simulations are performed strictly for two-dimensional geometry, while the experiments are performed with three-dimensional channels though the height dimension of  $7\ \mu\text{m}$  is a mere 2% of its width of  $300\ \mu\text{m}$ . Hence, electrokinetic flow in experiments is primarily driven by the top and bottom surfaces of the channels, while the simulated electro-osmotic flow is driven by the (infinitely long) side surfaces only. Despite this difference, comparisons between simulations and experiments show surprisingly good agreement, as will be seen extensively in the next section. This may be due to the fact that comparisons are made under steady Stokes flow conditions, where electrokinetic forces are balanced by viscous diffusion, which is isotropic. In addition, the  $\mu\text{-PIV}$  gives channel-height-averaged velocity measurements to average out any three-dimensional effects in the experimental results.

## 6 Results and discussions

In this section, detailed comparisons between numerical predictions and measurement data are presented for two different micro-channel configurations: (1) a straight channel with a groove of  $300\ \mu\text{m}$  by  $300\ \mu\text{m}$  (Fig. 4), and (2) a T-junction with asymmetric electrode configuration (Fig. 9). The grooved-channel creates a sudden perturbation in an electro-osmotically driven straight channel flow, and locally induces a two-dimensional electric field. This enables us to observe the effects of a two-dimensional

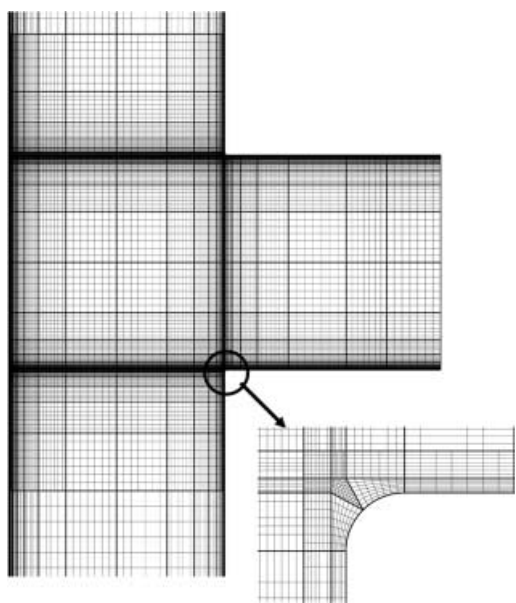


Fig. 4. The spectral element discretization used for the grooved micro-channel simulation, with magnified grid structure shown near the corner

electric field on electro-osmotic transport. The T-junction has three inlet/outlet ports, while two electrodes are placed so that a  $90^\circ$  turning flow is electro-osmotically driven, while the third inlet is left open to allow a small amount of induced flow. This configuration enables us to examine electro-osmotic transport in a micro-channel junction where the flow is turning.

### 6.1 Grooved-channel

Experiments are performed with a square groove in a micro-channel that is  $300\ \mu\text{m}$  wide and  $7\ \mu\text{m}$  deep. The electrodes are placed at the inlet and exit of the channel, and an electric field of  $10\ \text{V/mm}$  is applied in the  $\zeta$ -direction, as shown in Fig. 6. The  $\mu\text{-PIV}$  measurements showed an average velocity of  $350\ \mu\text{m/s}$  at both the inlet and exit sections of the domain. The zeta potential is estimated using Eq. 7, to be  $50\ \text{mV}$ . This experimentally determined zeta potential value is used as a boundary condition for numerical simulations.

Numerical simulation of electro-osmotic transport requires resolution of a sharp EDL region. The spectral element discretization of sharp corners is illustrated with a magnified grid structure in Fig. 4. We obtain grid independent solutions by successively increasing the expansion order. In this study, we used 9th-order modal expansions in each direction to resolve the EDL and the flow field. The actual computational domain extends 20 channel heights from the groove in both directions to accommodate fully developed steady flows. The volumetric flow rate, corresponding to a plug flow profile is imposed at the inflow, while zero Neumann boundary conditions are imposed at the outflow section. The Laplace equation, Eq. 6, is solved for the electric potential for the extended computational domain. Specified electric potential values are imposed at the extended inlet and exit, while zero Neumann conditions are imposed on all other channel surfaces. Figure 5 shows the calculated electric field and equal potential contour lines for the truncated grooved channel geometry. In order to show the dramatic changes near the sharp corners, we intentionally increased the electric-field-line density near the grooved side of the channel.

In Fig. 6, we present streamlines and velocity vectors of numerical and experimental results for the grooved micro-channel. The velocity vectors agree fairly well qualitatively and quantitatively. We observe a uniform plug-like flow in the upstream (A–A section) and downstream (D–D section) of the groove. In these regions the flow is unidirectional, while the flows near the groove corners show two-dimensional flow due to the flow turning. The resulting flows inside the groove (B–B and C–C sections) are highly two-dimensional. Note the similarities observed between the electric field lines (Fig. 5) and the calculated streamlines. This similarity indicates that the flow is a purely electro-osmotic driven flow, without being influenced by any hydrostatic pressure gradient. This was possible by attaching an over-sized reservoir to the inlet and by keeping the exit open to minimize build-up of hydrostatic pressure differential in the channel. The electric field is stronger near the first and the second corners

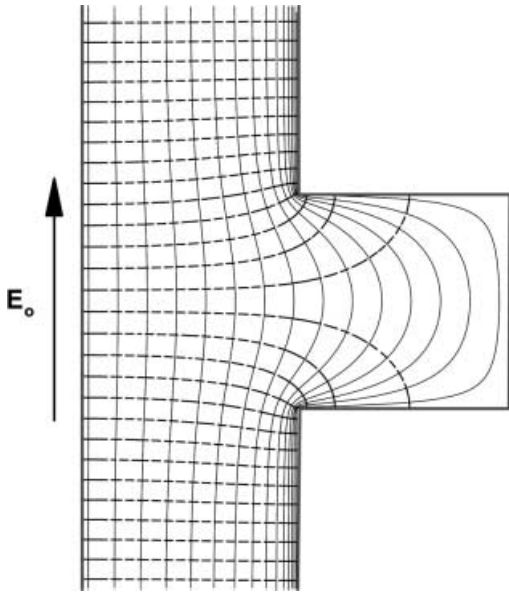


Fig. 5. Electric field lines (solid) and equal potential contour lines (dashed) in the grooved micro-channel

of the groove, which results in stronger electro-osmotic drive near these corners. Indeed, the streamwise velocity gradually increases along the channel wall as the flow approaches the first corner and decreases as the flow turns into the groove. For the second corner, the flow accelerates as it emerges from the groove and decelerates as it merges with the main stream.

Figure 7 shows quantitative comparisons of the streamwise velocity,  $U_\xi$ , at the incoming A-A section and outgoing D-D section. Both experimental and numerical results are normalized by a single value of the Helmholtz-Smoluchowski velocity, which is experimentally determined as  $U_{HS}=350 \mu\text{m/s}$  as shown in Eq. 7. The dimensionless ( $\xi, \eta$ ) coordinates are normalized by the channel half height  $h=150 \mu\text{m}$ . The numerical predictions (solid curves) and experimental results (the symbols connected by dashed lines) show close agreement with each other. Both velocity profiles at A-A and D-D show almost plug-like distribution with slight bias towards the channel wall on the groove side ( $\eta=+1$ ). This is due to the aforementioned increase in the electric field stress around the corners, which locally increases the electro-osmotic velocity near the corners of the grooved region.

Figure 8 shows the stream-wise velocity,  $U_\xi$ , and cross-stream velocity,  $U_\eta$ , at the sections B-B and C-C inside the groove. Owing to the sudden expansion, the cross-stream velocity ( $U_\eta$ ) becomes very prominent in this region. Since the electric field lines are parallel to the surface on the groove (see Fig. 5), the electric field interacts with the EDL, and creates large cross-stream velocity near the groove walls. Since the external electric field diminishes rapidly deeper down the groove, the flow field in section C-C is significantly weaker than in section B-B. The magnitude of cross-stream velocity ( $U_\eta$ ) at B-B is as high as 75% of the maximum streamwise velocity ( $U_\xi$ ) at the inlet, while at C-C it is as high as 25%. The streamwise velocity reaches its maximum at the center ( $\xi=0$ ), and its magnitude is

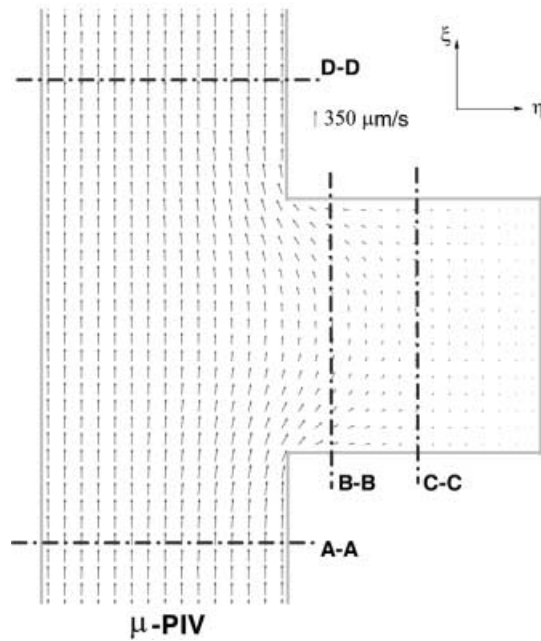
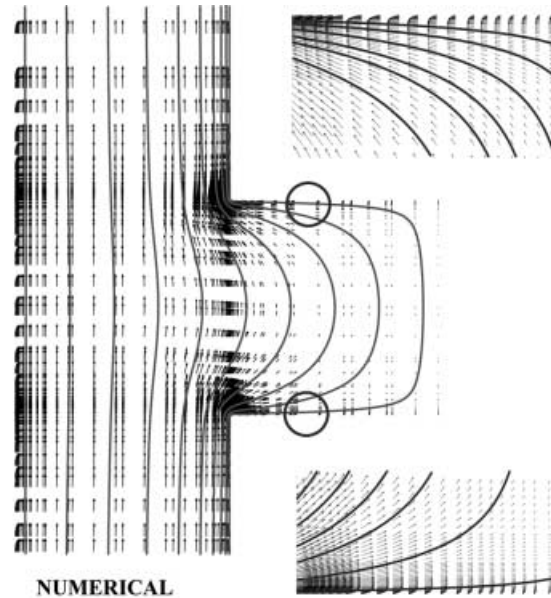


Fig. 6. Comparison of velocity vectors and streamlines between the  $\mu$ -PIV results (bottom) and the numerical results (top) for the grooved micro-channel

approximately 40% of the maximum streamwise velocity at B-B, while 20% at C-C.

## 6.2 T-junction

Experiments are performed at a T-junction of a micro-channel (Fig. 9). The channel is  $300 \mu\text{m}$  wide and  $7 \mu\text{m}$  deep, similar to the grooved channel. The positive electrode is placed at the inlet of the side-armed channel and the negative electrode is placed at the exit (the left end) of the straight channel. An electric field of  $10 \text{ V/mm}$  is applied between the two electrodes. A separate reservoir is attached at the end of each channel section to supply/discharge fluid. As the electro-osmotically driven flow is

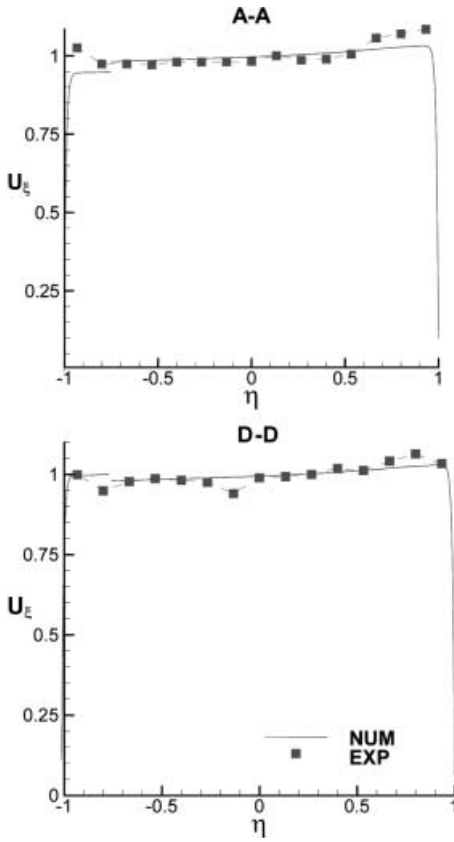


Fig. 7. Point-wise comparison of the stream-wise velocity,  $U_{\xi}$ , in the grooved micro-channel at A-A and D-D sections

continued, the height of the exit reservoir gradually increases, while the inlet reservoir height decreases. This builds up the hydrostatic pressure gradient in the opposite direction to the electro-osmotic flow. The resulting velocity profiles will be receded from the ideal electro-osmosis-driven plug flow by superposition of the adverse pressure-driven parabolic component. The measured volumetric flow rate is used to specify the inlet boundary condition for the numerical simulation to account for the adverse pressure gradient effect. Also the Helmholtz–Smoluchowski velocity of  $260 \mu\text{m/s}$  and zeta potential of  $37.7 \text{ mV}$  are calculated based on the experimental data.

The computational domain is again extended by 20 channel heights away from the junction in all three directions. The inlet boundary condition is specified so that the flow rate matches the measured data. The measured flow rate is lower than the flow rate that would have been achieved solely by electro-osmosis drive, because of the adverse pressure gradient. Thus, the imposition of the measured flow rate enables the numerical simulation to properly account for the effect of the adverse pressure gradient. Fully developed flow conditions, i.e., zero-Neumann boundary conditions, are specified at both ends of the horizontal channel section.

Close agreement is achieved in comparison with the measured and calculated velocity fields (Fig. 9). Flow coming from the inlet (top) turns left along the electric field direction. Both the experimental and the numerical results show an increase in the flow vectors along the left surface of the side channel, as the left corner is approached, and then a gradual decrease along the top wall of the straight channel toward the exit. Streamlines closer

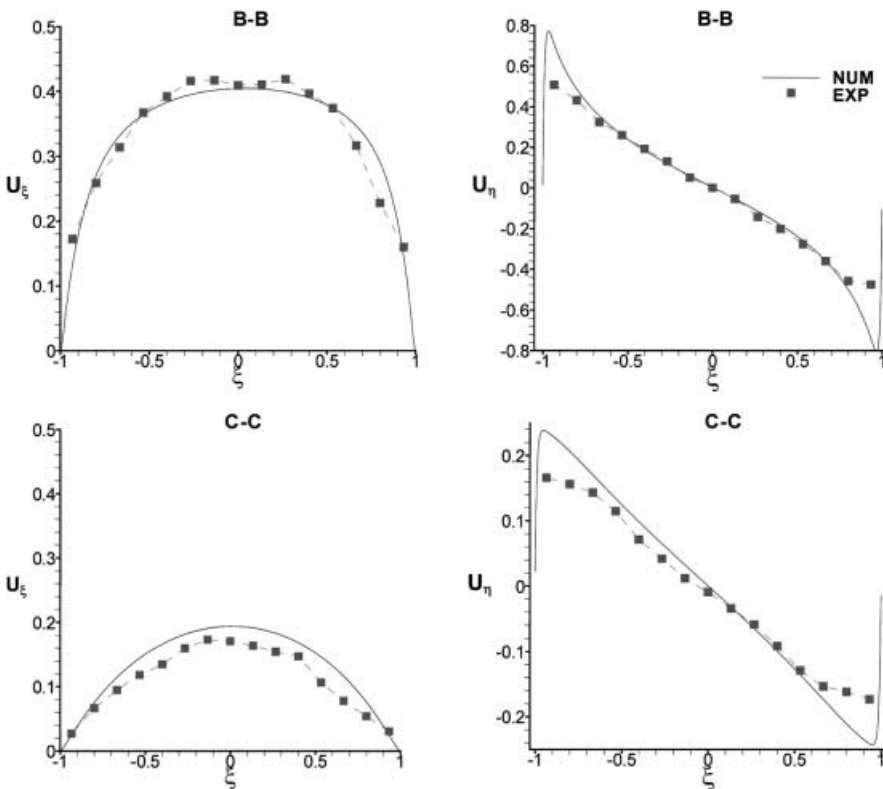


Fig. 8. Point-wise comparisons of the stream-wise velocity,  $U_{\xi}$ , and cross-stream velocity,  $U_{\eta}$ , in the grooved micro-channel at B-B and C-C sections

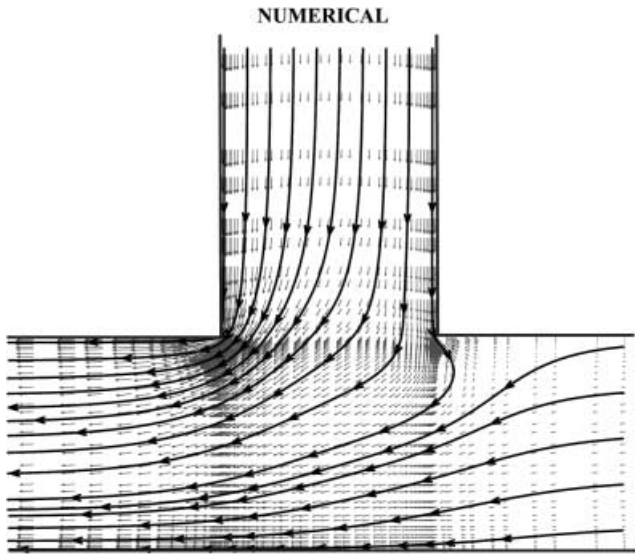


Fig. 9. Comparison of velocity vectors and streamlines between the  $\mu$ -PIV results and the numerical results for the T-junction micro-channel under asymmetric electro-osmosis drive

to the right surface expand toward the right horizontal channel, but they eventually turn left toward the bottom left exit. Both experimental and numerical results show induced flow from the right-hand side merging with the main stream and merging to the left exit. Though not presented, the computation shows that the static pressure at the junction is lower than the right and left reservoirs. This pressure differential induces the flow from the right reservoir to the junction. The junction pressure is calculated to be slightly higher than that at the inlet, and this is consistent with the adverse pressure gradient due to the hydrostatic differential between reservoirs and the junction, as shown in the measured and calculated velocity vectors.

Electric field lines are presented in Fig. 10. Zero Neumann conditions are imposed at the end of the right channel, while the electric potential is specified at the inlet and the left exit to simulate the two electrodes. The electric field lines are turning symmetrically with a large radius of

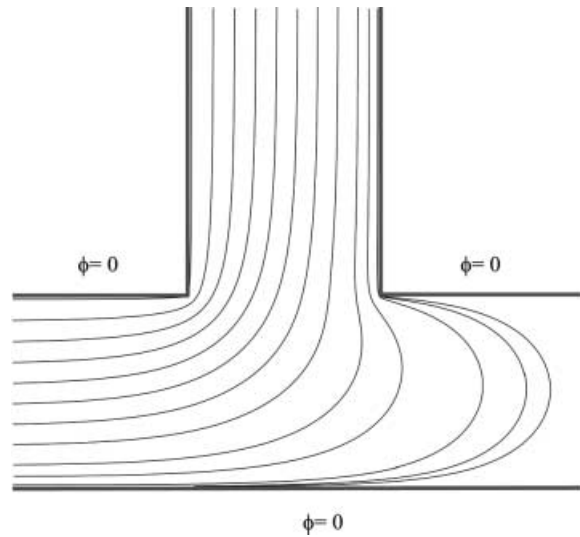
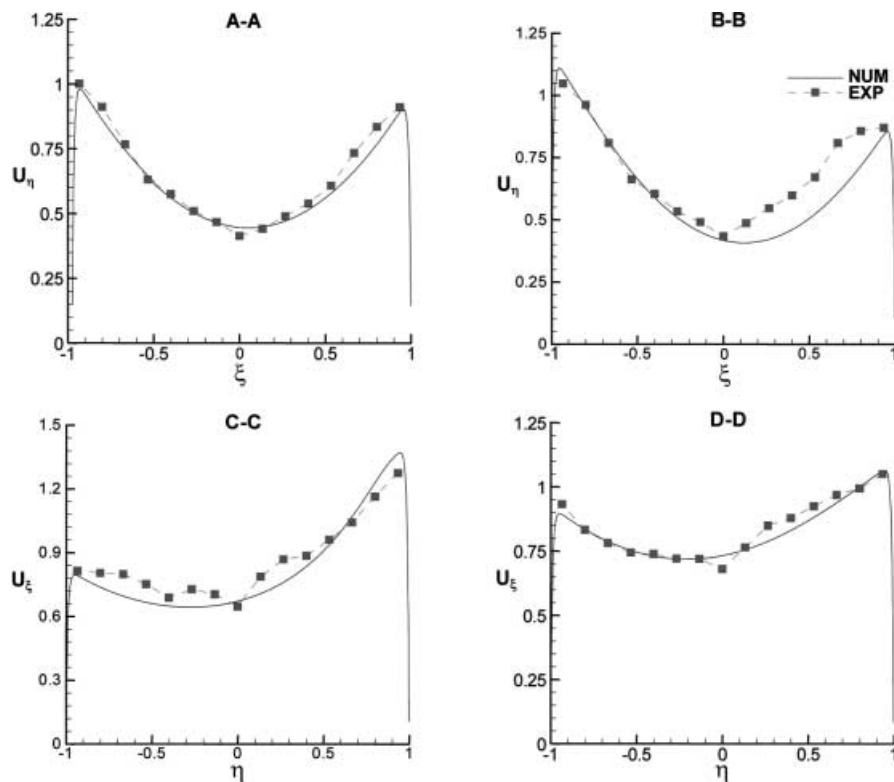


Fig. 10. Electric field lines computed in the T-junction region

curvature, while the streamlines presented in Fig. 9 exhibit sharper turns squeezed by the induced flow streams from the right reservoir. The flow streamline would have more closely followed the electric field lines in the absence of adverse pressure gradient, i.e., in the case of pure electro-osmotic driven flow where uniform pressure prevails. For the present superposed electro-osmotic/pressure case, weak similarity is observed between the electric field lines and the streamlines.

In Fig. 11, we present point-wise comparisons between the  $\mu$ -PIV results and simulations at four different locations for the T-junction geometry, as marked with four dashed lines in Fig. 9. Both experimental and numerical velocity vectors are normalized by the single measured average velocity of  $260 \mu\text{m/s}$  (Helmholtz-Smoluchowski velocity in Eq. 7). The streamwise velocity distribution at inlet A-A depicts the superposition of an adverse-parabolic velocity profile with a plug-like flow, with a slight asymmetry across the channel. The peak velocity is larger near the left surface ( $\xi=-1$ ) than that at the right surface ( $\xi=1$ ). Since the electric field is applied asymmetrically from top to left, its streamwise gradients are larger on the left corner than on the right corner, resulting in asymmetric electro-osmotic drive in the flow field. The increasing asymmetry at section B-B, which is closer to the T-junction, is attributed to the increased electric field near the corner. Also note that the velocity along the surface,  $\eta=-1$ , increases before the left corner (from A-A to B-B) and decreases after the corner (from C-C to D-D) as the electro-osmotic drive increases and then decreases around the corner.

Streamwise velocity distributions ( $U_{\xi}$ ) in the left channel, at two different locations C-C and D-D, show the superposed effect of the electro-osmotic driven flow with the adverse pressure-driven flow. The asymmetry of the latter is weakened compared with the former because the electric field is reduced away from the left corner. For the same reason, the velocity near the top surface ( $\eta=1.0$ ) of the left channel decreases from C-C to D-D, and the velocity near the bottom surface



**Fig. 11.** Point-wise comparisons of the stream-wise velocity,  $U_\eta$  (A-A and B-B sections) and  $U_\xi$  (C-C and D-D sections), for the T-junction micro-channel flow driven by asymmetric electro-osmosis

( $\eta = -1.0$ ) increases, recovering the flow symmetry. This is again because of the diminished asymmetry in the electric field as being away from the corner. Comparison of the velocity distributions at sections A-A and D-D show that the outgoing flow rate at the left channel (D-D) has been noticeably increased from the incoming flow rate (A-A), due to the merged addition of the induced flow from the right side of the channel. Therefore, the adverse pressure gradient effects on the velocity distribution at section D-D are less apparent compared with those at section A-A.

## 7

### Concluding remarks

Quantitative global and point-wise comparisons are presented between the experimental and numerical results for electro-osmotic flows through a grooved micro-channel and a T-junction geometry. Experiments were based on the use of a  $\mu$ -PIV technique, while the simulations utilized a high-order finite element formulation. Overall, good agreement between the experiments and numerical simulations are observed.

For both grooved and T-junction channels, we observed strong electric fields near the sharp corners, which resulted in an increase in the streamwise velocity near the corners. For pure electro-osmotic flow in a grooved-channel, in which no adverse pressure gradient is present, a high level of similarities is shown between the electric field lines and the computed streamlines. However, in the T-junction geometry, the similarity is weakened because of the effect of the adverse pressure gradients, between the inlet and exit reservoirs, and the induced suction from the right reservoir.

Note that the fabricated channel has an extremely shallow depth ( $7 \mu\text{m}$ ) and  $\mu$ -PIV, of which the imaging depth is estimated to be  $11.4 \mu\text{m}$ , measured depthwise averaging two-dimensional flow fields. The simulation is also based on two-dimensional governing equations. Most micro-flows, including the cases presented here, are confined between two parallel plates, similar to the Hele-Shaw apparatus. Hence, irrespective of the viscous nature of the flows, the streamlines obtained for these cases, with the proximity between the two plates ensured, resemble those of a corresponding potential flow.

To observe the truly three-dimensional nature of microscale electro-osmotic flows, a future development of a fully three-dimensional computational code is needed. Also, an extended fabrication of micro-channels with the channel depth comparable to its width will be needed to allow depthwise-resolved  $\mu$ -PIV measurements. For example,  $\mu$ -PIV associated with the optical sectioning capability of confocal microscopy can be utilized to investigate the three-dimensionality effects in electro-osmotically driven micro-flows in the future.

### References

- Adrian RJ (1997) Dynamic ranges of velocity and spatial resolution of particle image velocimetry. *Meas Sci Technol* 8:1393–1398
- Anderson JR, Chiu DT, Jackman RJ, Cherniavskaya O, McDonald JC, Wu H, Whitesides SH, Whitesides GM (2000) Fabrication of topologically complex three-dimensional microfluidic systems in PDMS by rapid prototyping. *Anal Chem* 72:3158–3164
- Born M, Wolf E (1965) *Principles of optics*. Pergamon Press, Oxford
- Bianchi F, Ferrigno A, Girault HH (2000) Finite element simulation of an electro-osmotic-driven flow division at a T-junction of microscale dimensions. *Anal Chem* 72:1987–1993
- Bianchi F, Wagner F, Hoffmann P, Girault HH (2001) Electroosmotic flows in composite microchannels and implications in micro-capillary electrophoresis systems. *Anal Chem* 73:829–836

- Burgreen D, Nakache R (1964) Electrokinetic flow in ultrafine capillary silts. *J Phys Chem* 68:1084–1091
- Cummings EB (1999) PIV measurement of electro-osmotic and pressure-driven flow components in microfluidic systems. *Proc ASME MEMS vol 1, Microelectromechanical Systems*:377–384
- Cummings EB, Griffiths SK, Nilson RH (1999) Irrotationality of uniform electro-osmosis. *Proc SPIE Microfluidic Devices Syst II*:180–189
- Dutta P, Beskok A (2001a) Analytical solution of combined electro-osmotic/pressure driven flows in two-dimensional straight channels: finite Debye layer effects. *Anal Chem* 73:1979–1986
- Dutta P, Beskok A (2001b) Time periodic electro-osmotic flows: analogies to Stokes' second problem. *Anal Chem* 73:5097–5102
- Dutta P, Warburton TC, Beskok A (2002a) Numerical simulation of mixed electro-osmotic/pressure driven micro flows. *Numer Heat Transfer A* 41:131–148
- Dutta P, Warburton TC, Beskok A (2002b) Electroosmotic flow control in complex micro-geometries. *J Microelectromech Syst* 11:36–44
- Einstein A (1905) *Ann D Phys* 17; this and related articles by Einstein have been translated and reprinted in: R. Furth (ed) (1956) *Investigations on the theory of Brownian movement*. Dover, New York
- Ermakov SV, Jacobson SC, Ramsey JM (1998) Computer simulations of electrokinetic transport in microfabricated channel structure. *Anal Chem* 70:4494–4505
- Friedlander SK (1977) *Smoke, dust and haze*. Wiley, New York
- Herr AE, Molho JI, Santiago JG, Mungal MG, Kenny TW, Garguilo MG (2000) Electroosmotic capillary flow with nonuniform zeta potential. *Anal Chem* 72:1053–1057
- Inoue S, Spring KR (1997) *Video microscopy*, 2nd edn. Plenum Press, Oxford
- Mala GM, Li D, Werner C, Jacobasch HJ, Ning YB (1997) Flow characteristics of water through a microchannel between two parallel plates with electrokinetic effects. *Int J Heat Fluid Flow* 18:489–496
- Meinhart CD, Wereley ST, Santiago JG (1999) PIV measurements of a microchannel flow. *Exp Fluids* 27:414–419
- Mitchell MJ, Qiao R, Aluru NR (2000) Meshless analysis of steady-state electro-osmotic transport. *J Microelectromech Syst* 9:435–449
- Nann T, Heinze J (1999) Simulation in electrochemistry using the finite element method. Part 1. The algorithm. *Electrochem Commun* 1:289–294
- Ohshima H; Kondo T (1990) Electrokinetic flow between two parallel plates with surface-charge layers-electro-osmosis and streaming potential. *J Colloid Interface Sci* 135:443–448
- Olsen MG; Adrian RJ (2000) Out-of-focus effects on particle image visibility and correlation in microscopic particle image velocimetry. *Exp Fluids* 29:S166–S174
- Overbeek JTG (1952) Phenomenology of lyophobic systems. In: Kruyt HR (ed) *Colloid science*, vol 1. Elsevier, Amsterdam, pp 58–59
- Patankar NA, Hu HH (1998) Numerical simulation of electro-osmotic flow. *Anal Chem* 70:1870–1881
- Probstein RF (1994) *Physicochemical hydrodynamics*. John Wiley, New York
- Rice CL, Whitehead R (1965) Electrokinetic flow in a narrow cylindrical capillary. *J Phys Chem* 69:4017–4023
- Reuss FF (1809) Notice sur un nouvel effet de l'électricité galvanique. *Mem Soc Impe Nat Moscou* 2:327–336
- Santiago J (2001) Electroosmotic flow in microchannels with finite inertial and pressure forces. *Anal Chem* 73:2353–2365
- Santiago JG, Wereley ST, Meihart CD, Beebe DJ, Adrian RJ (1998) A particle image velocimetry system microfluidics. *Exp Fluids* 25:316–319
- Yang C, Li D, Masliyah JH (1998) Modeling forced liquid convection in rectangular microchannels with electrokinetic effect. *Int J Heat Mass Transfer* 41:4229–4249